**THE EUROPEAN
PHYSICAL JOURNAL E**

Regular Article - Living Systems

On the fluid drag reduction in scallop surface

Botong Li[1], Zitian Zhao[1], Linyu Meng[1], and Liangliang Zhu[2,a]

[1] School of Mathematics and Physics, University of Science and Technology Beijing, Beijing 100083, China
[2] School of Chemical Engineering, Northwest University, Xi'an 710127, China

Abstract In the field of biomimetics, the tiny riblet structures inspired by shark skin have been extensively studied for their drag reduction properties in turbulent flows. Here, we show that the ridged surface texture of another swimming creature in the ocean, i.e., the scallops, also has some friction drag reduction effect. In this study, we investigated the potential drag reduction effects of scallop shell textures using computational fluid dynamics simulations. Specifically, we constructed a conceptual model featuring an undulating surface pattern on a conical shell geometry that mimics scallop. Simulations modeled turbulent fluid flows over the model inserted at different orientations relative to the flow direction. The results demonstrate appreciable friction drag reduction generated by the ribbed hierarchical structures encasing the scallop, while partial pressure drag reduction exhibits dependence on alignment of scallop to the predominant flow direction. Theoretical mechanisms based on classic drag reduction theory in turbulence was established to explain the drag reduction phenomena. Given the analogous working environments of scallops and seafaring vessels, these findings may shed light on the biomimetic design of surface textures to enhance maritime engineering applications. Besides, this work elucidates an additional evolutionary example of fluid drag reduction, expanding the biological repertoire of swimming species.

1 Introduction

The maneuvering of objects within turbulent fluid flows elicits significant drag forces, stemming from viscosity, and pressure differentials enhanced by vortical structures and chaotic motions arising in the surrounding flow field. The mitigation of such drag forces, through creative control strategies and surface modifications, can yield substantial gains in energy efficiency with importance across diverse transportation, defense, and engineering sectors. Therefore, researchers have proposed and developed various drag reduction strategies, such as microbubble drag reduction [1, 2], vibrant wall drag reduction [3], coating drag reduction [4, 5], polymer additive drag reduction [6, 7], and so on.

As our best teacher, nature has already provided us ingenious ways of drag reduction in fluid flow [8]. One example is the use of guar gum, a natural polymer, which can significantly decrease the friction drag in turbulent flows when added in small concentrations [9, 10]. Another example is the dolphin, which has special adaptations such as eye secretions and a compliant skin that helps to lower the fluid drag [11, 12]. Furthermore, the shark, the fastest swimming animal in the ocean, has a skin that exhibits remarkable drag

reduction properties [13]. The skin is composed of dermal denticles, which are shaped like tiny aligned riblets and can reduce the drag by up to 9.9% [14]. Interestingly, some fast-swimming shellfish in the ocean also has macroscopic longitudinal ribs on their hard shells, showing an undulating pattern on the surface. This raises the question of whether this specific structure has a beneficial effect on drag reduction during their swimming motion.

Contrary to the common assumption that seashells are sessile organisms that remain attached to the ocean floor [15], some species of sea scallops exhibit remarkable swimming abilities [16]. For instance, the sea (or giant) scallop can reach a velocity of 0.79 m/s, while the saucer scallop can attain up to 1.6 m/s. These impressive feats can be observed in many online videos. Examples include Crazy scallops [17] and Swimming Bay Scallops Homosassa Florida [18]. The swimming performance of these scallops is attributed to both biological factors (such as strong muscles) and physical factors (such as the grooved surface of their shells). In this work, we will explore and analyze how the shell morphology contributes to the drag reduction in turbulent flow from a mechanical perspective.

Fluid drag forces imparted on bodies moving through fluids fundamentally consist of two components: viscous friction drag arising from shear at surfaces, and pressure drag caused by imbalanced force on frontal versus rear aspects. In many systems such as maritime vessels and

a e-mail: zhu.liangliang@nwu.edu.cn (corresponding author)

pipe conduits, friction drag constitutes the majority of performance losses, accounting for approximately 70% and almost 100% of the total drag budget, respectively [19]. Under normal circumstances in turbulence, friction drag in turbulent flows increases with greater surface area exposed to shearing flow interactions. Hence, traditionally smoother surfaces were pursued to minimize drag. However, pioneering work at NASA in the early 1980s [20, 21] revealed that specifically engineered surface riblet structures (micro-ridges and grooves) could substantially reduce turbulent skin friction. The mechanism of riblet drag reduction remains complex with ongoing investigations [22, 23], but prevailing hypotheses suggest that riblets modify near-wall turbulence to retain high-velocity vortices above ridge crests while enabling low-velocity flow in grooves over most of the surface area [24]. Extensive research has since focused on optimizing riblet geometries in terms of height, spacing, cross-sectional shape, and orientations to maximize drag reduction for different applications [25, 26], through numerical [27–29] or experimental efforts [30, 31]. Findings to date imply that small variations in geometry can profoundly impact drag reduction efficacy [32], necessitating multi-parameter analyses using numerical simulations and experimental flow diagnostics.

This present investigation explores the drag reduction properties of scallop shell with an undulatory morphology of macroscopic longitudinal ribs, using biomimetic modeling and numerical fluid simulations. Scallops represent an intriguing natural prototype for such studies, as their ridged shells enable swift swimming driven by multiple opening modes for propulsion and steering. We employ computational fluid dynamics (CFD) to examine if these pronounced surface structures also confer drag reducing abilities, specifically targeting skin friction versus pressure drag components. Our methodology firstly extracts a conceptual model from a sea scallop, which features an undulating surface on a conical shell geometry. It merits clarification that the hierarchical ridge-valley features encasing scallops differ markedly in dimensions from previous micro- and nano-structured riblet investigations in physical scale and absolute values. By evaluating fluid flows over this conceptual model textured by macroscopic riblets and undulations, we can determine if analogous surface patterns produce friction and/or pressure drag reductions for this biological system. Findings will elucidate scallops as a potential biological source of relatively large-scale nature-derived drag reduction mechanisms for marine engineering to enhance mobility and efficiency of submarines and seafaring vessels.

2 Models and methods

2.1 Model descriptions

To simulate the hydrodynamic performance of scallops, we developed a conceptual model based on their sizes and dimensions [33] and placed it in a rectangular water channel (Fig. 1a). The model consists of a conical-shaped structure with undulating patterns (longitudinal ribs) on the surface. The specific parameters for the rectangular channel and the ridged conical model are given in Fig. 1b and c, respectively. In addition, we also constructed a smooth conical model without riblet structure (Fig. 1d) for comparison purposes .
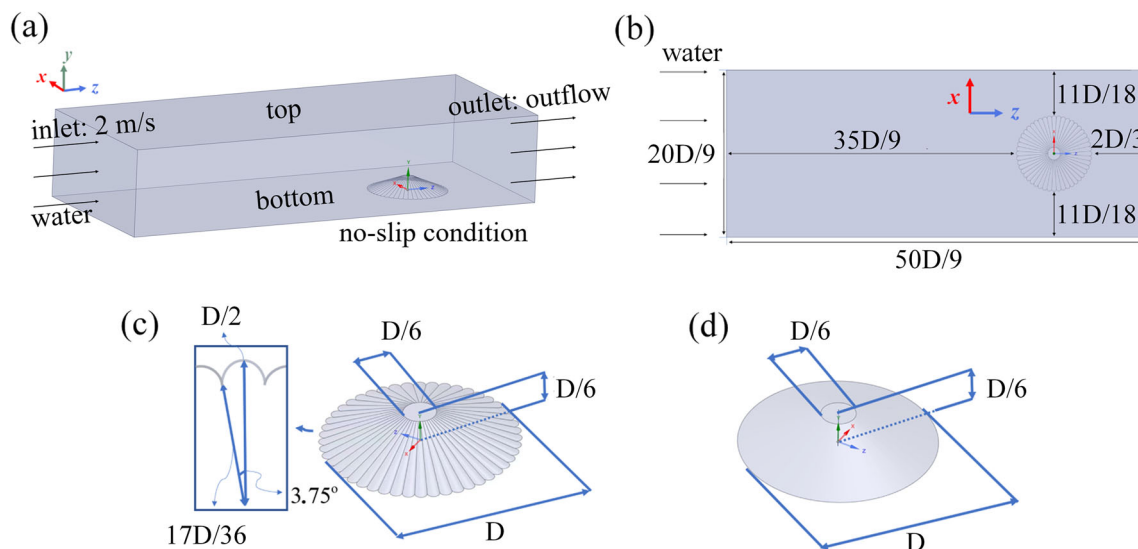
Fig. 1 Geometries of the simulation model: **a** three-dimensional configuration of the water channel with a conical model placed at the bottom, **b** two-dimensional top view of the water channel, and three-dimensional configuration, and **c** the ridged conical model, and **d** the smooth conical model. $D = 90$ mm
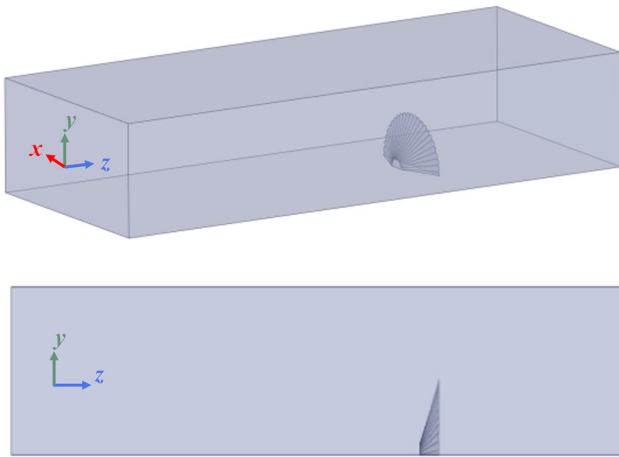
Fig. 2 Configuration of the conical model vertically placed in the rectangular channel

When considering biological factors that support the design of our model's morphology, we primarily relied on a biology study [33] which offers detailed descriptions in terms of size of the shell, and the number, and shape of the ridges. For example, the diameter of an actual shell (referred to as shell length in ref. [33]) is primarily within the range of 80–110 mm, thus we deemed it apt to choose 90 mm as the bottom diameter (D) for our ideal shell model. Moreover, with regard to the number and shape of ridges, ref. [33] observed approximately 12 clearly discernible ridges within a 90-degree shell sector. Based on this observation, we have incorporated 48 ridges in our ridged conical model, ensuring a proportional and anatomically accurate representation. The shape of each ridge is also based on measurements and data obtained in ref. [33].

To investigate the drag reduction effect from another perspective, the conical model was oriented vertically with respect to the direction of the water flow in the rectangular channel (see Fig. 2). For computational efficiency, only half of the conical model was simulated.

The choice of the above two orientations was grounded in the two distinct states of movement exhibited by scallops in their natural marine environment: the state of attachment to the seabed and the state of free-living. For the former, we primarily relied on a study [15] that provides detailed insights into the relationship between the orientation of scallop shells in their daily life and the direction of water currents. It is mentioned in ref. [11] that, the water current direction is parallel to the inhalant and exhalant streams of the scallop. To be consistent with that, our conical model was thus firstly placed horizontally in the rectangular channel. For the latter, with reference to refs. [17] and [18] which offer a visual representation of a scallop shell moving in a posture perpendicular to the water flow.

The meshing of the models was performed using the Workbench ICEM CFD software, which employs unstructured grids to accommodate the irregular shape of the conical models, particularly the ridged conical model (Fig. 1c). The resulting meshes are shown in Fig. 3.

2.2 Governing equations

For stable incompressible three-dimensional turbulence, the Reynolds-averaged Navier–Stokes equations are adopted as follows:

Continuity equation:

$$\frac{\partial u_i}{\partial x_i} = 0 \tag{1}$$

Momentum equation:

$$\frac{\partial}{\partial x_j}(\rho u_j u_i) = -\frac{\partial P}{\partial x_i} + \frac{\partial}{\partial x_j}\left(\mu\left(\frac{\partial u_i}{\partial x_j} + \frac{\partial u_j}{\partial x_i}\right) - \rho\overline{u_i' u_j'}\right) \tag{2}$$

where ρ is the water density; u_i and u_i' represent the components of time-averaged and instantaneous velocity in the i direction, respectively ($i = 1, 2, 3$ represent x, y, z in Cartesian coordinates, respectively). P is the pressure, and μ is the viscosity coefficient.

The standard $k-\varepsilon$ model is adopted, which are determined by solving the following equations:

Turbulence kinetic energy equation:

$$\rho u_j \frac{\partial k}{\partial x_j} = \sigma_{ij} \frac{\partial u_i}{\partial x_j} - \rho\varepsilon + \frac{\partial}{\partial x_j}\left(\left(\mu + \frac{\mu_T}{\sigma_k}\right)\frac{\partial k}{\partial x_j}\right) \tag{3}$$

Turbulence dissipation rate equation:

$$\rho u_j \frac{\partial \varepsilon}{\partial x_j} = C_{\varepsilon 1}\frac{\varepsilon}{k}\sigma_{ij}\frac{\partial u_i}{\partial x_j} - C_{\varepsilon 2}\rho\frac{\varepsilon^2}{k} + \frac{\partial}{\partial x_j}\left(\left(\mu + \frac{\mu_T}{\sigma_\varepsilon}\right)\frac{\partial \varepsilon}{\partial x_j}\right) \tag{4}$$

where k is the turbulence kinetic energy and ε is the turbulence dissipation. $\sigma_{ij} = \mu_T(\partial u_i/\partial x_j + \partial u_j/\partial x_i)$ is expressed as Reynolds stress tensor and $\mu_T = \rho C_\mu(k^2/\varepsilon)$ is the turbulence viscosity. $C_{\varepsilon 1}$, $C_{\varepsilon 2}$, C_μ, σ_k and σ_ε are empirical constants, and the values are $C_{1\varepsilon} = 1.44$, $C_{2\varepsilon} = 1.92$, $C_\mu = 0.09$, $\sigma_k = 1.0$ and $\sigma_\varepsilon = 1.3$, respectively, in the current simulation.

The inlet of the computational domain is defined as a velocity inlet and the velocity magnitude is set to 2 m/s. This particular relative velocity of water and shell is determined according to Joll's work [34], where the saucer scallop, *Amusium balloti*, can swim at a speed of 1.6 m/s. The Reynolds number for the simulations is approximately 265,273. The type of the outlet is considered as outflow, and no-slip condition is applied to all wall boundaries. The commercial CFD software ANSYS Fluent is used in simulations. In the pressure–velocity coupling algorithm, second-order upwind scheme is used in the discrete schemes for accuracy of results.

Fig. 3 Grids of **a** the computational domain and **b** the ridged conical model

(a)

(b)
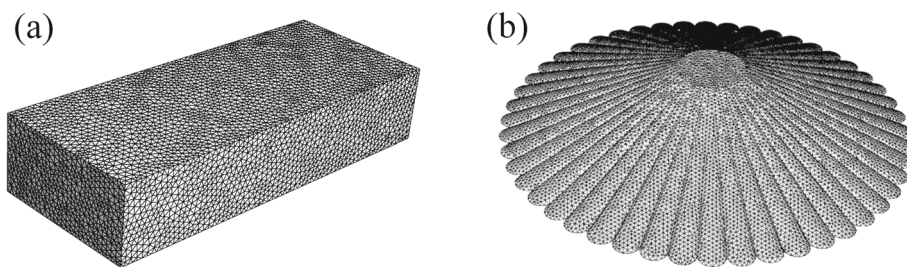
Table 1 Mesh configuration

Name	Nodes	Elements
Mesh #1	56,983	332,706
Mesh #2	86,566	498,459
Mesh #3	97,030	547,620
Mesh #4	199,763	1,129,096
Mesh #5	324,329	1,836,980

2.3 Validation

In order to find the appropriate grid, five meshes of different sizes are constructed as indicated in Table 1.

Pressure value on the intersection line of the conical shell model and plane $x = 0$ is used to evaluate the mesh quality. The pressure value at the maximum of z is used as the reference value to normalize all the pressure data. With different meshes on the conical shell model, pressure curves of the line at $x = 0$ are obtained and shown in Fig. 4a. It can be seen that the five pressure curves are almost the same, and in the following simulation, Mesh #4 is adopted. The curves of residual variation with iteration number are depicted in Fig. 4b. It can be seen that the results are convergent within the allowable ranges of errors. When the calculated residual values reach 10^{-3} or less, the residual curves remain steady.

3 Results and discussions

3.1 Wall shear on conical models

The resistance encountered by the shell in water is mainly the friction drag and the pressure drag, which are focused in this and the following sections. Data on the crest and trough of each ridge on the surface of the ridged conical shell model are extracted from the simulations. As shown in Fig. 5a, 96 lines are marked on the surface of the shell, where the odd-numbered lines correspond to the crests and the even-numbered lines correspond to the troughs. The angular distance between two adjacent lines is 3.75°. For comparison, lines are also drawn at the same locations on the smooth conical shell model (Fig. 5b). The results along each line are averaged to a single value to reveal the average effect.

Friction drag generates with the velocity gradient between a fluid and an object that are in relative motion. The velocity gradient induces a shear stress at the object's wall, which is the local expression of friction drag. Figure 5c shows the distributions of normalized wall shear on the ridged conical model and the smooth conical model. To compare the effects of different geometries on the hydrodynamic performance of the conical model, we used the average shear stress at Line 24 of the ridged conical shell model as a reference value. Line 24 is located on the ridged conical model at the trough behind the water flow, as shown by the white dashed line in Fig. 5a. The ridged conical shell model exhibits a "W" shape in both the crest and valley lines, with three local maxima and two minima along the downstream direction (from Line 1 to Line 49). The crest lines have generally higher shear stress than the trough lines, except for the region around Line 24, where the crest and trough lines have similar shear stress. This region corresponds to the part of the conical shell that is obscured. The presence of a large vortex in the wake region may induce the local maxima of the shear stress. The higher velocity gradients at the crests may account for the larger shear stress at the crest lines.

The smooth model (Fig. 5b) shows that the shear stress curves of the crest and trough lines are almost identical due to the lack of surface roughness. The shear stress curves have a double "V" shape from Line 1 to 96, with two local minima (at Lines 25 and 73) and three local maxima (at Lines 1, 49, 96). A notable finding is that the wall shear stress of the ridged conical model is considerably lower than that of the smooth model, especially for the trough lines. This can be explained by the existing theories of friction drag reduction mechanisms of roughness in turbulent flows. The vortices that form on the surface of the ridged shell stay above the convexity tips, creating low velocities in the valleys. These regions have lower velocity gradients than those over the smooth shell, resulting in a significant reduction in shear stress over most of the surface.

We further investigated the drag reduction effects of the ridged structure on the half conical shell vertically placed in the rectangular channel (see Fig. 2). Here, 49 lines are marked for extracting the data as shown in Fig. 6a and b. The normalized wall shear for both the ridged and smooth half conical models is presented in Fig. 6c. Again, the average shear stress at Line 24 on the ridged half conical model was used as the reference value.
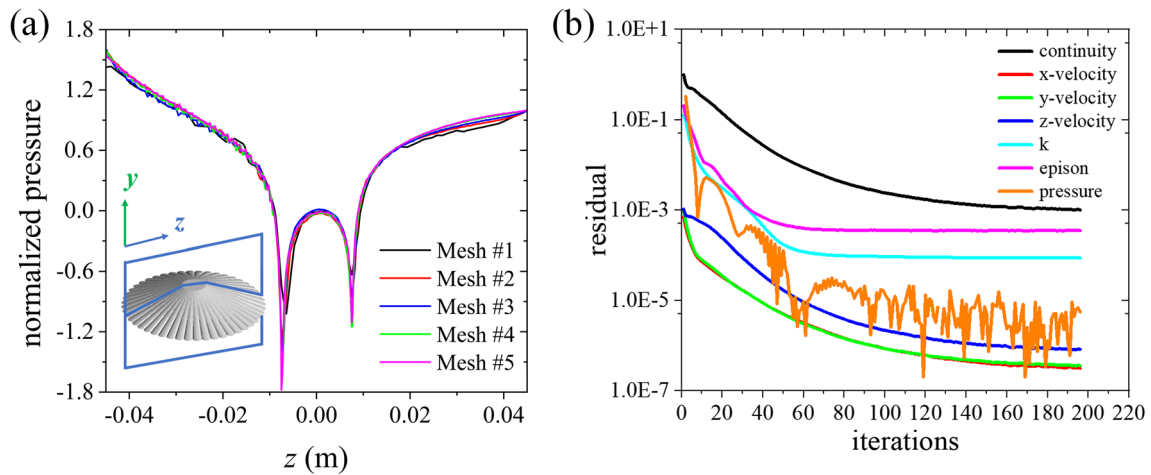
Fig. 4 a Pressure data of one line on the ridged conical model with different mesh sizes, and **b** residual monitoring where the pressure data were the average value of all pressure exerted on the surface of the shell model

Fig. 5 Lines used for shear stress and pressure data extraction of **a** the ridged conical shell model, and **b** the smooth conical model, and **c** normalized wall shear of these lines on both models. In (a) and (b), several lines are highlighted (white dashed lines) for better illustration of the location of different lines
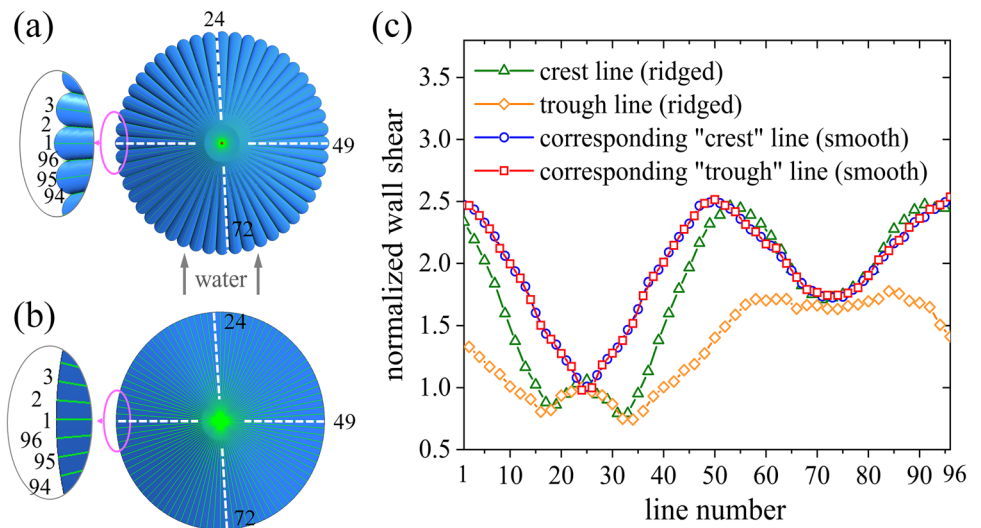
Fig. 6 Lines used for shear stress and pressure data extraction of **a** the ridged half conical model, and **b** the smooth half conical model, and **c** normalized wall shear of these lines on both models. Both models are placed vertically in the rectangular channel (see Fig. 2)

(a)

(b)

ridged model   smooth model
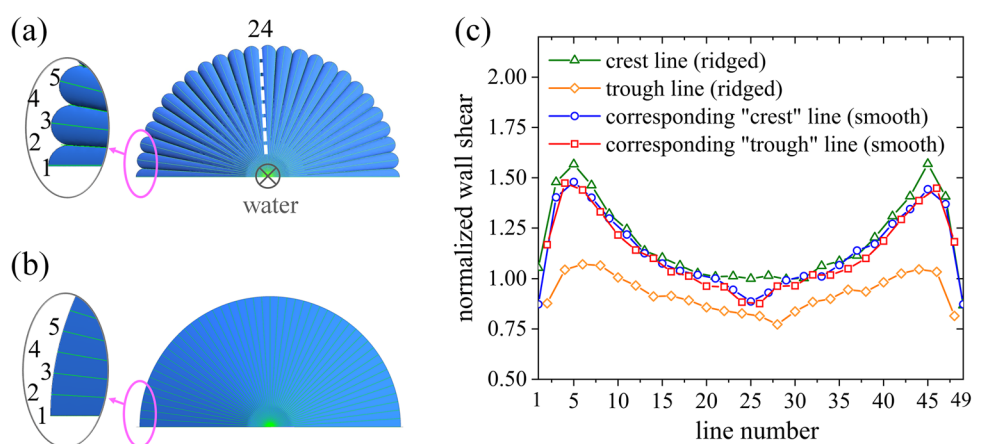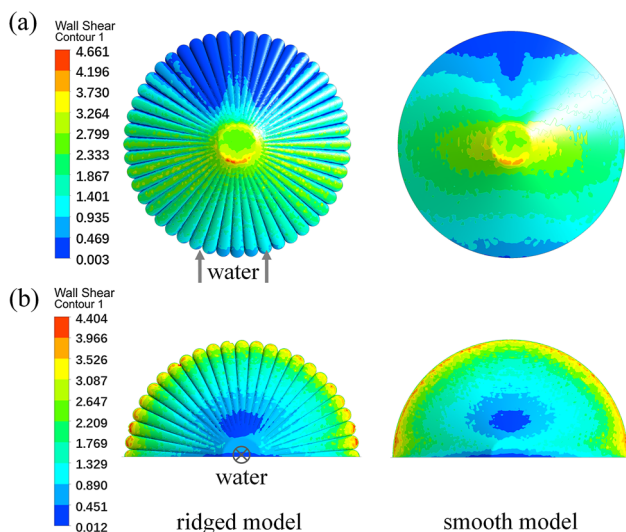
Fig. 7 Normalized wall shear stress contours of **a** horizontal and **b** vertical (half) conical ridged/smooth models

A comparison between Figs. 6c and 5c reveals that the normalized wall shear decreases significantly when the conical model is placed vertically. The reason for this is that the main resistance force shifts from friction drag to pressure drag, which leads to a gradual reduction in wall shear. We also hypothesize that the pressure should increase under this condition, which is later verified. Another observation is that the vertical ridged half conical model shows little difference in shear stress at crest lines relative to the smooth model, while notable difference is still present in trough lines. As explained by Lee et. al's work [35], the lower shear in the valley implies that the cross-stream velocity fluctuations inside the valley are much smaller than those over a smooth surface, which corresponds to a decrease in wall shear.

To illustrate the shear distribution, we show the wall shear stress contours of the horizontally (Fig. 1) and vertically (Fig. 2) placed (half) conical models with and without ridges in Fig. 7. Similar to Fig. 5c, the average shear stress at Line 24 of the ridged conical shell model is used as the reference value. For the horizontal models (Fig. 7a), the smooth conical model has a larger low-shear zone at the upstream region (which faces the water direction) than the ridged conical model, due to the smaller surface area and thus lower friction drag of the smooth conical model. However, at the downstream region (which hides behind the water direction), the surface area effect is less significant and the lower velocities on the ridged conical model result in lower wall shears. For both horizontal (Fig. 7a) and vertical (Fig. 7b) models, we observe that the ridged models have larger low-shear-stress zones than the smooth ones, indicating that the ridged models have less resistance to wall shear force than the smooth models.

3.2 Pressure on conical models

In this section, we will examine another type of fluid drag, namely the pressure drag, which occurs when the water in front of an object flows around it due to the relative motion between the water and the object. The pressure drag is caused by the non-uniform pressure distribution on the surface of the object, which is the main variable of interest in our analysis in this section. We use the same data selection method as in the previous section, and we adjust the reference pressure value to the mean pressure value at Line 1 on the ridged conical model.
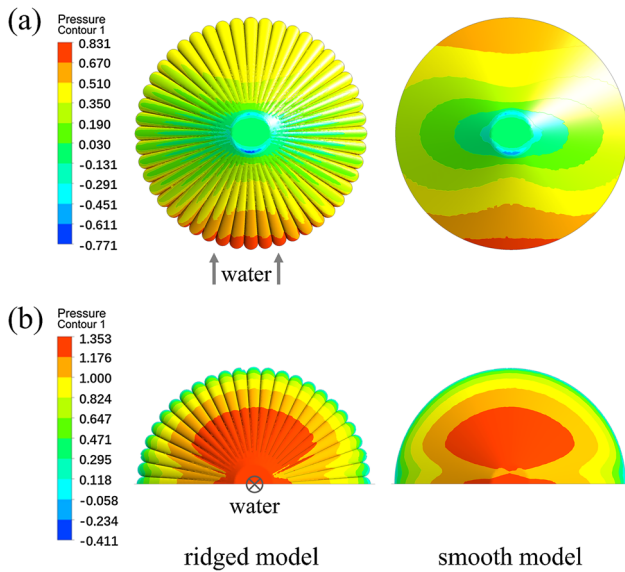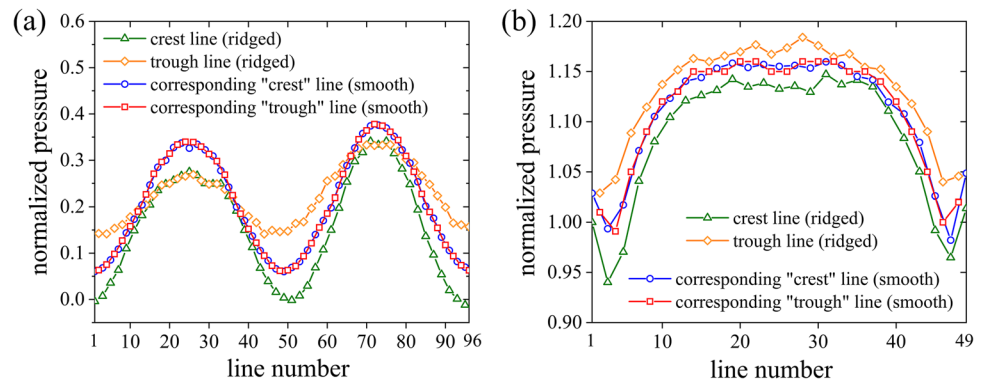
Figure 8 shows the normalized pressure distribution for the conical models. For the horizontal conical model with ridges (Fig. 1), we still observed a degree of pressure reduction effect of the ridged structure. The pressure in the troughs from Line 1 to 49 is generally smaller than that of the corresponding regions of the smooth model, while for Line 50 to 96, it is generally larger (Fig. 8a). The pressure at the crests of the ridged conical model is also lower than that of the smooth model all the way from Line 1 to 96 (Fig. 8a). For the vertical half conical model with ridges (Fig. 2), the water flow is perpendicular to the shell surface, and the water discharge from the troughs is greater than that of the corresponding regions of the smooth model, leading to higher pressure in the troughs and lower pressure on the crests (Fig. 8b). Overall, for the vertical half conical model, the ridged structure has a negligible effect on reducing the pressure on the shell surface.

To visualize the pressure distribution in a more direct way, we present the pressure contours of different models in Fig. 9. Similar to Fig. 8, the mean pressure value at Line 1 on the ridged conical model is used as the reference value. The most noticeable difference in the horizontal conical models is that the pressures on the downstream side (back of the conical model) are much lower for the ridged model than for the smooth model, which agrees with the results in Fig. 8a. For the vertical half conical models, the pressure contours are very similar for both types of shells, and no significant differences are observed. Another interesting phenomenon is that, due to the vortex shedding on the shell surface, some small negative pressure zones (dark blue zones) appear, where the shell surface experiences suction. However, we did not detect any negative values in the previous analysis on wall shear.

3.3 Limitations and future research

The current study only considers the drag characteristics of a shell under two orientations at one Reynolds number, while a scallop could face more complex water flow situations. Besides, scallops have many kinds of surface morphologies and their sizes may vary in a wide range. In future research, different surface morphologies and roughness of shells can be studied, and more shell

Fig. 8 Normalized pressure of **a** the horizontal conical ridged/smooth models and **b** vertical half conical ridged/smooth models

Fig. 9 Normalized pressure contours of **a** horizontal and **b** vertical (half) conical ridged/smooth models

direction. These findings accord with established theoretical mechanisms of turbulent drag manipulation via structured micro-surface geometries. Specifically, the ridged features along scallop shells resemble traditional engineered riblet structures, appearing to keep high-velocity turbulent flows on the crests while fostering regions of low shear in the grooves. Beyond elucidating the functionality behind scallop shell shapes, these bio-inspired surface patterns could see engineering implementations for maritime applications requiring drag reduction enhancements. As conceptual prototypes, our biomimetic models extracted key geometric aspects of scallop shells to replicate their capabilities of damping turbulent fluid flows. Such nature-inspired surface designs could be refined using simulations to balance multifunctional pressures of structural integrity, mobility constraints, and fluid dynamic performance. In summary, scallops present an as yet untapped biological source of turbulent drag reduction mechanisms of potential utility to marine engineering across domains from cargo transport to navigation.

Author contribution statement

Conceptualization was contributed by Liangliang Zhu, Botong Li; methodology was contributed by Botong Li, Zitian Zhao; Formal analysis and investigation were contributed by Zitian Zhao, Botong Li, Linyu Meng, Liangliang Zhu; writing—original draft preparation, was contributed by Zitian Zhao, Botong Li, Liangliang Zhu; writing—review and editing, was contributed by Botong Li, Liangliang Zhu.

Data availability The raw data can be obtained on request from the corresponding author.

Declarations

Conflict of interest The authors have no relevant financial or non-financial interests to disclose.

sizes and orientation angles can be considered to explore the influence of angle on drag reduction effect. Moreover, submergence depth, wave amplitude, and velocity of the submersible in the sea affect the load characteristics [36]. Similarly, scallops in the sea may also be affected by these factors, which can be taken into account in future research.

4 Conclusions

This investigation assessed whether the pronounced surface morphology of scallop shells confers drag reduction capabilities to scallops in turbulent flows. Using biomimetic models and computational fluid dynamics (CFD) simulations of external flows over shell textures, appreciable friction drag reduction was demonstrated largely independent of angle of water flow. Partial pressure drag reduction also exhibited dependence on the alignment of the scallop model to the predominant flow

Fig. 10 Models with different computational domain sizes: **a** 500 × 400 × 200 mm^3 and **b** 500 × 300 × 150 mm^3. **c** Pressure data of one line on the ridged conical model with different computational domain sizes. The dimensions of domain #1, #2, and #3 are 500 × 300 × 150 mm^3, 500 × 400 × 200 mm^3, and 500 × 200 × 100 mm^3, respectively
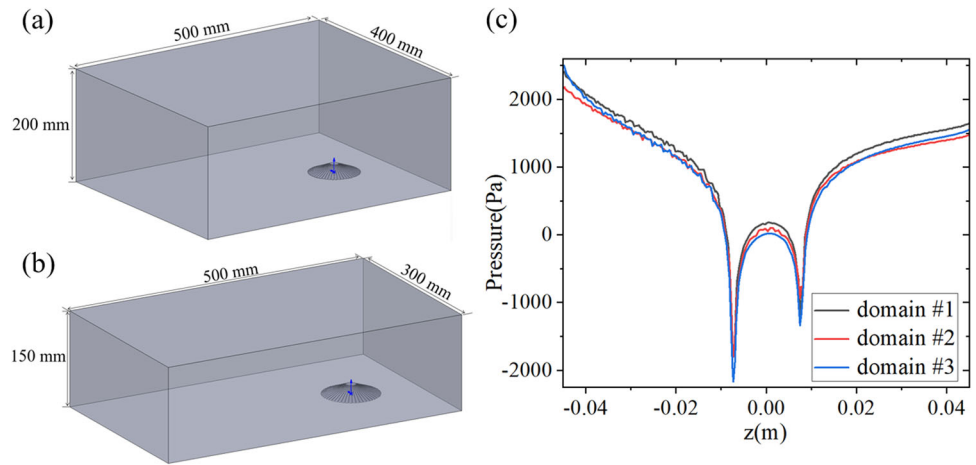
Appendix 1

Domain independence analysis was conducted to demonstrate that the calculation results are independent of the computational domain sizes. In addition to the computational domain mentioned above, we also constructed two additional models with different computational domain sizes as shown in Fig. 10. Following the approach outlined in Sect. 2.3, we utilized the pressure value at the intersection of the conical shell model and the plane $x = 0$ (see inset in Fig. 4a) as a benchmark. With different computational domains on the conical shell model, pressure curves of the line at $x = 0$ were obtained and shown in Fig. 10c. It can be seen that the three pressure curves are almost the same, thus showing the independence of the results on the domain size.

Appendix 2

An uncertainty analysis and evaluation were conducted on the chosen grid. The horizontally positioned shell model depicted in Fig. 1a was utilized, and the average wall shear stress across the entire shell surface was assessed. Three distinct grids were selected, and the grid size was adjusted using a refinement ratio of 1.5. The number of grid elements and the corresponding wall shear stress values is detailed in Table 2.

Table 2 Total element number and wall shear value for uncertainty analysis

Grid	Number	Wall shear (N)
Fine	1,129,096	11.1
Medium	764,751	10.5
Coarse	498,459	9.38

The convergence ratio is calculated based on the following formula [37]:

$$Ri = \frac{S_{i2} - S_{i1}}{S_{i3} - S_{i2}} = \frac{\varepsilon_{i,21}}{\varepsilon_{i,32}} \quad \text{(A1)}$$

The convergence ratio determines the convergence type based on specific conditions as follows:

(a) Monotonic convergence for $0 < R_i < 1$,
(b) Oscillatory convergence for $-1 < R_i < 0$,
(c) Monotonic divergence for $1 < R_i$,
(d) Oscillatory divergence for $R_i < -1$.

If R_i is between 0 and 1, the error ($\delta^*_{i,1}$), the order of accuracy (p_i), and the correction factor (C_i) by using the generalized Richardson Extrapolation (RE) can be evaluated as follows:

$$\delta^*_{i,1} = C_i \delta^*_{\text{RE}i,1} \quad \text{(A2)}$$

$$\delta^*_{\text{RE}i,1} = \frac{\varepsilon_{i,21}}{r_i^{p_i} - 1} \quad \text{(A3)}$$

$$p_i = \frac{\ln\left(\frac{\varepsilon_{i,32}}{\varepsilon_{i,21}}\right)}{\ln(r_i)} \quad \text{(A4)}$$

$$c_i = \frac{r_i^{p_i - 1}}{r_i^{p_{i,est} - 1}} \quad \text{(A5)}$$

The uncertainty (U_i) and the corrected uncertainty (U_{Ci}) can be calculated as:

$$U_i = (|C_i| + |1 - C_i|)\left|\delta^*_{\text{RE}i,1}\right| \quad \text{(A6)}$$

$$U_{Ci} = |1 - C_i|\left|\delta^*_{\text{RE}i,1}\right| \quad \text{(A7)}$$

The uncertainty quantification parameters (R_i, $\delta^*_{i,1}$, $\delta^*_{\text{RE}i,1}$, p_i, C_i, U_{Ci}) are provided in Table 3.

Table 3 Grid sensitivity data for the verification of wall shear

R_i	$\delta^*_{i,1}$	$\delta^*_{REi,1}$	p_i	C_i	U_{Ci}
0.536	-0.480	-0.692	1.539	0.693	0.212

The shear stress parameters on the wall exhibit Monotonic convergence relative to the grid refinement, with R_i value between 0 and 1.

References

1. Y.Y. Feng, H. Hu, G.Y. Peng, Y. Zhou, Microbubble effect on friction drag reduction in a turbulent boundary layer. Ocean Eng. **211**, 107583 (2020). https://doi.org/10.1016/j.oceaneng.2020.107583

2. H. Yang, Z. Guo, Y. Li, H. Wang, Y. Dou, Experimental study on microbubble drag reduction on soil-steel interface. Appl. Ocean Res. **116**, 102891 (2021). https://doi.org/10.1016/j.apor.2021.102891

3. J.Z. Zhao, G. Pan, S. Gao, Research on the mechanism of drag reduction by wall vibration through Lattice Boltzmann method. Mod. Phys. Lett. B **34**(27), 2050295 (2020). https://doi.org/10.1142/s0217984920502954

4. Q. Mao, J. Zhao, Y. Liu, H.J. Sung, Drag reduction by a flexible hairy coating. J. Fluid Mech. **946**, A5 (2022). https://doi.org/10.1017/jfm.2022.594

5. L.C. Li, B. Liu, H.L. Hao, L.Y. Li, Z.X. Zeng, Investigation of the drag reduction performance of bionic flexible coating. Phys. Fluids (2020). https://doi.org/10.1063/5.0016074

6. X. Zhang, X.L. Duan, Y. Muzychka, Degradation of flow drag reduction with polymer additives—a new molecular view. J. Mol. Liq. **292**, 111360 (2019). https://doi.org/10.1016/j.molliq.2019.111360

7. T. Kouser, Y. Xiong, D. Yang, Contribution of superhydrophobic surfaces and polymer additives to drag reduction. ChemBioEng Rev. **8**(4), 337–356 (2021). https://doi.org/10.1002/cben.202000036

8. S. Alben, M. Shelley, J. Zhang, Drag reduction through self-similar bending of a flexible body. Nature **420**(6915), 479–481 (2002). https://doi.org/10.1038/nature01232

9. M.V. Lisboa Motta, E.V. Ribeiro de Castro, E.J. Bassani Muri, B.V. Loureiro, M.L. Costalonga, P.R. Filgueiras, Thermal and spectroscopic analyses of guar gum degradation submitted to turbulent flow. Int. J. Biol. Macromol. **131**, 43–49 (2019). https://doi.org/10.1016/j.ijbiomac.2019.03.037

10. D. Kulmatova, F. Hadri, S. Guillou, D. Bonn, Turbulent viscosity profile of drag reducing rod-like polymers. Eur. Phys. J. E Soft Matter **41**, 1–6 (2018). https://doi.org/10.1140/epje/i2018-11751-3

11. T.I. Jozsa, E. Balaras, M. Kashtalyan, A.G.L. Borthwick, I.M. Viola, Active and passive in-plane wall fluctuations in turbulent channel flows. J. Fluid Mech. **866**, 689–720 (2019). https://doi.org/10.1017/jfm.2019.145

12. A. Roccon, F. Zonta, A. Soldati, Turbulent drag reduction by compliant lubricating layer. J. Fluid Mech. **863**, R1 (2019). https://doi.org/10.1017/jfm.2019.8

13. B. Dean, B. Bhushan, Shark-skin surfaces for fluid-drag reduction in turbulent flow: a review. Philos. Trans. Math. Phys. Eng. Sci. **368**, 1933–5737 (2010). https://doi.org/10.1098/rsta.2010.0294

14. D.W. Bechert, M. Bruse, W. Hage, J.G.T. Van Der Hoeven, G. Hoppe, Experiments on drag reducing surfaces and their optimization with an adjustable geometry. J. Fluid Mech. **338**, 59–87 (1997). https://doi.org/10.1017/S0022112096004673

15. A.R. Brand, in *Scallops: Biology, Ecology, Aquaculture, and Fisheries*, ed. by Sandra E. Shumway, G. Jay Parsons (Elsevier, 2016), p. 469 https://doi.org/10.1016/B978-0-444-62710-0.00011-0

16. J.L. Manuel, M.J. Dadswell, Swimming of juvenile sea scallops, *Placopecten magellanicus* (Gmelin): a minimum size for effective swimming? J. Exp. Mar. Biol. Ecol. **174**, 137–175 (1993). https://doi.org/10.1016/0022-0981(93)90015-G

17. https://www.youtube.com/watch?v=kw6wGwKEdT8

18. https://www.youtube.com/watch?v=NBH3UvlZo90

19. D.M. Bushnell, J.N. Hefner, *Viscous Drag Reduction in Boundary Layers* (American Institute of Aeronautics and Astronautics, Washington DC, 1990). https://doi.org/10.2514/4.865978

20. M.J. Walsh, L.M. Weinstein, Drag and heat-transfer characteristics of small longitudinally ribbed surfaces. AIAA J. **17**, 770–771 (1979). https://doi.org/10.2514/3.61216

21. M.J. Walsh, Riblets as a viscous drag reduction technique. AIAA J. **21**, 485–486 (1983). https://doi.org/10.2514/3.60126

22. W. Ran, A. Zare, M.R. Jovanovic, Model-based design of riblets for turbulent drag reduction. J. Fluid Mech. **906**, A7 (2021). https://doi.org/10.1017/jfm.2020.722

23. D. Gatti, M. Quadrio, Reynolds-number dependence of turbulent skin-friction drag reduction induced by spanwise forcing. J. Fluid Mech. **802**, 553–582 (2016). https://doi.org/10.1017/jfm.2016.485

24. H. Choi, P. Moin, J. Kim, Direct numerical simulation of turbulent flow over riblets. J. Fluid Mech. **255**, 503 (1993). https://doi.org/10.1017/s0022112093002575

25. F.J. Mawignon, J. Liu, L. Qin, A.N. Kouediatouka, Z. Ma, B. Lv, G. Dong, The optimization of biomimetic sharkskin riblet for the adaptation of drag reduction. Ocean Eng. **275**, 114135 (2023). https://doi.org/10.1016/j.oceaneng.2023.114135

26. T. Kim, R. Shin, M. Jung, J. Lee, C. Park, S. Kang, Drag reduction using metallic engineered surfaces with highly ordered hierarchical topographies: nanostructures on micro-riblets. Appl. Surf. Sci. **367**, 147–152 (2016). https://doi.org/10.1016/j.apsusc.2016.01.161

27. H. Qiu, K. Chauhan, C. Lei, A numerical study of drag reduction performance of simplified shell surface microstructures. Ocean Eng. **217**, 107916 (2020). https://doi.org/10.1016/j.oceaneng.2020.107916

28. S.T. Jose, K.K. Patra, S. Panda, Modeling and simulation of capillary ridges on the free surface dynamics of third-grade fluid. Z. für Naturforschung A **76**, 217–229 (2021). https://doi.org/10.1515/zna-2020-0225

29. K.K. Patra, S. Panda, Formation of the capillary ridge on the free surface dynamics of second-grade fluid over an inclined locally heated plate. Z. für Naturforschung

A **74**, 1099–1108 (2019). https://doi.org/10.1515/zna-2019-0126

30. G. Cafiero, G. Iuso, Drag reduction in a turbulent boundary layer with sinusoidal riblets. Exp. Therm. Fluid Sci. **139**, 110723 (2022). https://doi.org/10.1016/j.expthermflusci.2022.110723

31. B. Xu, H. Li, P. Lv, X. Liu, X. Tan, Y. Zhao, H. Duan, Effect of micro-grooves on drag reduction in Taylor–Couette flow. Phys. Fluids (2023). https://doi.org/10.1063/5.0145900

32. K.S. Choi, Fluid dynamics–the rough with the smooth. Nature **440**, 754 (2006). https://doi.org/10.1038/440754a

33. I. Tremblay, H.E. Guderley, J.H. Himmelman, Swimming away or clamming up: the use of phasic and tonic adductor muscles during escape responses varies with shell morphology in scallops. J. Exp. Biol. **215**, 4131–4143 (2012). https://doi.org/10.1242/jeb.075986

34. L.M. Joll, Swimming behaviour of the saucer scallop *Amusium balloti* (Mollusca: Pectinidae). Mar. Biol. **102**, 299–305 (1989). https://doi.org/10.1007/BF00428481

35. S.J. Lee, S.H. Lee, Flow field analysis of a turbulent boundary layer over a riblet surface. Exp. Fluids **30**, 153–166 (2001). https://doi.org/10.1007/s003480000150

36. L. Cheng, C. Wang, B. Guo, Q. Liang, Z. Xie, Z. Yuan, X. Chen, H. Hu, P. Du, Numerical investigation on the interaction between large-scale continuously stratified internal solitary wave and moving submersible. Appl. Ocean Res. **145**, 103938 (2024). https://doi.org/10.1016/j.apor.2024.103938

37. A.Z. Saydam, G.N. Küçüksu, M. İnsel, S. Gökçay, Uncertainty quantification of self-propulsion analyses with Rans-Cfd and comparison with full-scale ship trials. Brodogradnja **73**, 107–129 (2022). https://doi.org/10.21278/brod73406